Shear velocity structure of central Eurasia from inversion of surface wave velocities

A. Villaseñor [a],*, M.H. Ritzwoller [a], A.L. Levshin [a], M.P. Barmin [a], E.R. Engdahl [a], W. Spakman [b], J. Trampert [b]

[a] *Department of Physics, University of Colorado, Campus Box 390, Boulder, CO 80309, USA*
[b] *Faculty of Earth Sciences, University of Utrecht, Budapestlaan 4, 3584 CD Utrecht, The Netherlands*

Abstract

We present a shear velocity model of the crust and upper mantle beneath central Eurasia by simultaneous inversion of broadband group and phase velocity maps of fundamental-mode Love and Rayleigh waves. The model is parameterized in terms of velocity depth profiles on a discrete $2° \times 2°$ grid. The model is isotropic for the crust and for the upper mantle below 220 km but, to fit simultaneously long period Love and Rayleigh waves, the model is transversely isotropic in the uppermost mantle, from the Moho discontinuity to 220 km depth. We have used newly available a priori models for the crust and sedimentary cover as starting models for the inversion. Therefore, the crustal part of the estimated model shows good correlation with known surface features such as sedimentary basins and mountain ranges. The velocity anomalies in the upper mantle are related to differences between tectonic and stable regions. Old, stable regions such as the East European, Siberian, and Indian cratons are characterized by high upper-mantle shear velocities. Other large high velocity anomalies occur beneath the Persian Gulf and the Tarim block. Slow shear velocity anomalies are related to regions of current extension (Red Sea and Andaman ridges) and are also found beneath the Tibetan and Turkish–Iranian Plateaus, structures originated by continent–continent collision. A large low velocity anomaly beneath western Mongolia corresponds to the location of a hypothesized mantle plume. A clear low velocity zone in v_{SH} between Moho and 220 km exists across most of Eurasia, but is absent for v_{SV}. The character and magnitude of anisotropy in the model is on average similar to PREM, with the most prominent anisotropic region occurring beneath the Tibetan Plateau. © 2001 Elsevier Science B.V. All rights reserved.

Keywords: Eurasia; Surface waves; Velocity structure; Crust; Upper mantle; Transverse isotropy

1. Introduction

This paper presents a new, high-resolution shear velocity model for the crust and upper mantle of central Eurasia, obtained by inversion of broadband surface-wave group and phase velocities. We have two main motivations for conducting this study. First, knowledge of the regional structure of the Eurasian crust and upper mantle is fundamental for understanding the tectonic framework and mantle dynamics, posing constraints on possible models of geodynamic evolution. Second, knowledge of the seismic velocity structure is necessary to determine seismic event locations accurately and, therefore, for monitoring the Comprehensive Nuclear-Test-Ban Treaty (CTBT). The effect of crustal and upper mantle structure is especially important for locating small events, which are recorded only at regional distances. At these close distances body waves propagate exclusively in the crust and upper mantle, their travel times are affected by strong lateral heterogeneities in this region, and

* Corresponding author. Fax: +1-303-492-7935.
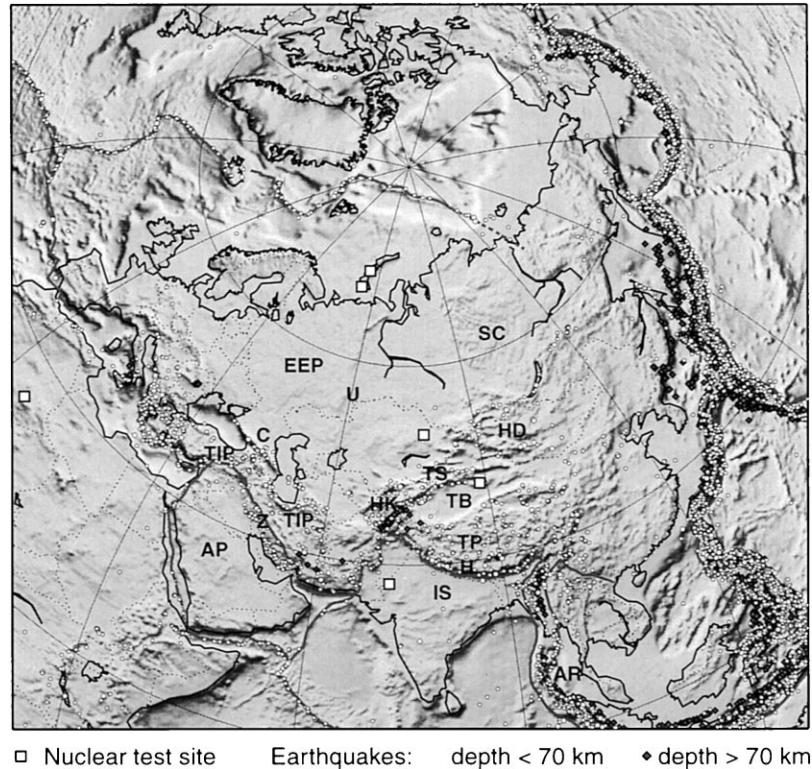*E-mail address:* antoniov@colorado.edu (A. Villaseñor).

Fig. 1. Location map of the studied region. Earthquake hypocenters are from the dataset of Engdahl et al. (1998). Note the high level of diffuse intraplate seismicity extending from the eastern Mediterranean to southeast Asia. White squares show the location of nuclear test sites in the region. AP: Arabian Peninsula; AR: Andaman ridge; C: Caucasus; EEP: East European platform; H: Himalaya; HD: Hangay dome; HK: Hindu–Kush; IS: Indian shield; SC: Siberian craton; TB: Tarim basin; TIP: Turkish–Iranian Plateau; TP: Tibetan Plateau; TS: Tien-Shan; U: Urals; Z: Zagros.

are poorly predicted by one-dimensional Earth models. The Eurasian continent is a natural choice for this type of seismic study. It provides a unique opportunity to study ongoing processes related to continental growth and collision and, from the CTBT monitoring viewpoint, central Asia is an important and challenging region. A number of nuclear test sites are located in regions of significant structural complexity in central Asia (Fig. 1). The study of Eurasia using seismic methods benefits from the Earth's largest intraplate seismic activity, related to the continent–continent collision occurring along the Tethyan orogen (Fig. 1).

Eurasia is the Earth's largest continent, and contains large regions which have been assembled over the last 500 million years. Morphologically it is composed of an assemblage of micro-plates and cratons, separated by mountain ranges or fold belts. The most

important event in the recent tectonic history of the continent is the Indo-Asian collision, responsible for the formation of the Himalayas and the Tibetan Plateau. This collision, initiated about 50 million years ago when the northward moving Indian plate collided with Asia (Searle et al., 1987), still continues and provides the opportunity for testing models of continental collision dynamics and continent formation. A large number of researchers have studied the seismic structure of central Asia, and particularly the Tibetan Plateau (see Molnar (1988) and Ritzwoller and Levshin (1998) for a review). Tomographic body wave studies have proven successful in imaging mantle structures, such as subducted slabs, back-arc basins and plumes. However, they provide limited information on crustal and uppermost mantle structure, especially in regions without seismic sources and/or

receiving stations. Therefore, the structure of large regions of stable Eurasia has not been imaged by body wave studies. Surface wave tomography allows us to fill in these gaps and to improve constraints in the crust and uppermost mantle. Recent advancements in seismic instrumentation and the installation of high-quality regional networks has improved the quality and resolution of surface wave studies.

2. Data

The data used in this study consist of surface-wave group and phase velocity maps. These maps represent the local group or phase velocity of the fundamental-mode Rayleigh or Love wave at each period, and have been obtained by tomographic inversion of group and phase velocity measurements (dispersion curves). The Rayleigh wave velocity maps used in this study range in period from 15 to 200 s, and from 15 to 150 s for Love waves.

The group velocity maps used in this study are based on the dataset of Ritzwoller and Levshin (1998). The original dataset has been increased by a factor of three, by incorporating newly processed measurements. We have compiled waveform data for events in Eurasia and along the surrounding plate boundaries from global broadband seismograph networks (GSN, Geoscope) and regional networks (CDSN, KAZNET, KNET, MEDNET). Group velocity dispersion curves were measured manually by analysts using the frequency–time analysis method (FTAN) of Levshin et al. (1992). Vertical component seismograms were used to measure Rayleigh wave dispersion, and horizontal component seismograms rotated to the transverse component were used for Love waves. This has resulted now into more than 29,000 measured Rayleigh wave dispersion curves, and more than 22,500 Love wave dispersion curves across Eurasia (20,000 Rayleigh measurements and 16,500 Love measurements inside the model region). The bandwidth of each measurement depends on the ability of the analyst to identify the direct fundamental-mode arrival. At short periods (below 30 s), this arrival may be obscured by scattered waves and multipathing. For longer periods the fundamental mode may be poorly excited, particularly for events with magnitudes smaller than 5.0. It is particularly

difficult to obtain high quality measurements for long period Love waves. This procedure results in a different number of measurements for each period, wave type, and location, and consequently a variable resolution of the maps. Fig. 2 illustrates the differences in ray-path coverage for Love and Rayleigh waves with periods of 50 and 100 s.

Phase velocity maps have been obtained from the dataset of Trampert and Woodhouse (1995), recently expanded with new measurements. Unlike the group velocity dataset of Ritzwoller and Levshin (1998), this is a global dataset, derived exclusively from global networks (GSN, Geoscope). The measurement method is automatic and is described in detail by Trampert and Woodhouse (1995). The period range of all measured dispersion curves is identical (40–150 s) resulting in the same data coverage for all periods (Fig. 2). The complete dataset comprises 23,000 measurements for Rayleigh waves, and 16,000 for Love waves. Because this is a global dataset, the ray-path coverage reflects the distribution of global seismicity and global broadband networks, with the highest path density in the northwest Pacific area (Fig. 2). On the other hand, the dataset of Ritzwoller and Levshin (1998) exhibits its highest path density in central Asia due to the choice of seismic sources and the existence of dense regional networks (e.g. KNET, Kazakh network, Tibetan Plateau PASSCAL array, etc.).

Because of the distribution of earthquakes and seismic stations, both datasets exhibit considerable redundancy, due to very similar paths. This allows consistency tests, outlier rejection, and the estimation of measurement uncertainties (Ritzwoller and Levshin, 1998). In this procedure ("cluster analysis") measurements with very similar ray paths are binned to produce a cluster or summary ray, resulting in a reduced, cleaner dataset. After this procedure the resulting group velocity dataset consists of 14,000 measurements for Rayleigh waves and 12,000 for Love waves. The phase velocity dataset is reduced to 16,000 Rayleigh wave measurements and 11,000 for Love waves distributed worldwide.

Rather than utilizing the group and phase velocity maps obtained by Ritzwoller and Levshin (1998) and Trampert and Woodhouse (1995) we have estimated new maps using their datasets (both original datasets have been expanded with new measurements). The reason is the different parameterization and properties
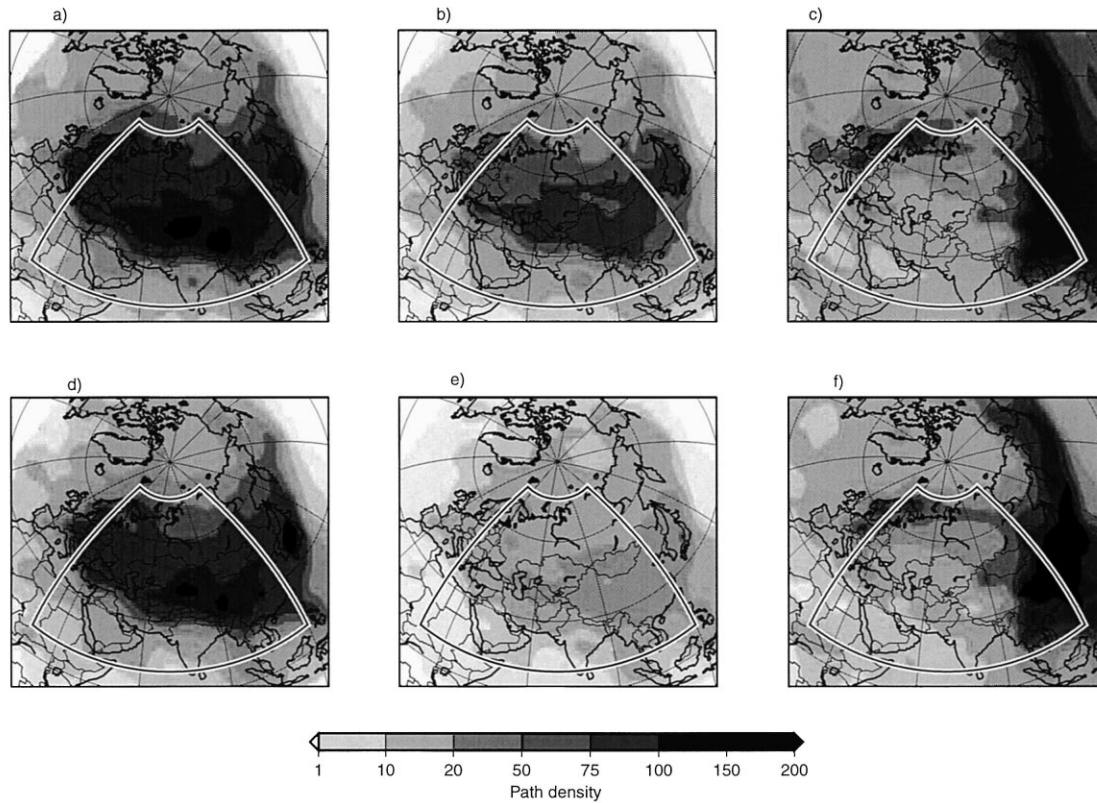
Fig. 2. Path density maps for group and phase velocity for the following waves and periods: (a) 50 s Rayleigh wave group velocity; (b) 100 s Rayleigh wave group velocity; (c) 50–150 s Rayleigh wave phase velocity; (d) 50 s Love wave group velocity; (e) 100 s Love wave group velocity and (f) 50–150 s Love wave phase velocity. Path density is defined as the number of great circle ray paths that cross each $2° \times 2°$ cell. For group velocities, path density maps are different for each wave type and period. For phase velocities, the distribution of paths for each wave type is identical for the entire period band of the measurements (50–150 s).

of the two sets of maps. In order to invert phase and group velocity maps simultaneously, it is desirable to make their characteristics more homogeneous. The group velocity maps of Ritzwoller and Levshin (1998) were obtained on a $2° \times 2°$ grid using the method of Yanovskaya and Ditmar (1990). This method is a generalization to two dimensions of a classical one-dimensional Backus–Gilbert approach, and sphericity is approximated by an inexact earth flattening transformation. On the other hand, the maps of Trampert and Woodhouse (1995) were parameterized in terms of a spherical harmonic expansion up to degree and order 40. We use the tomographic inversion method of Barmin et al. (2000) to obtain new group and phase velocity maps on a $2° \times 2°$ grid.

This method uses spherical geometry, applies spatial smoothing constraints, and allows for the estimation of spatial resolution and amplitude bias of the tomographic images. Examples of the newly obtained group and phase velocity maps are shown in Fig. 3. Surface wave velocity maps have been obtained for the following periods: Rayleigh group velocities at 15, 20, 25, 30, 40, 50, 60, 70, 80, 90, 100, 125, 150, 175, and 200 s; Love group velocities for the same periods only up to 150 s; and Love and Rayleigh phase velocities at 50, 60, 70, 80, 90, 100, 125, and 150 s. These surface wave dispersion maps are the data used to invert for shear velocity structure, amounting to a total of 44 velocity data for each geographical grid point.
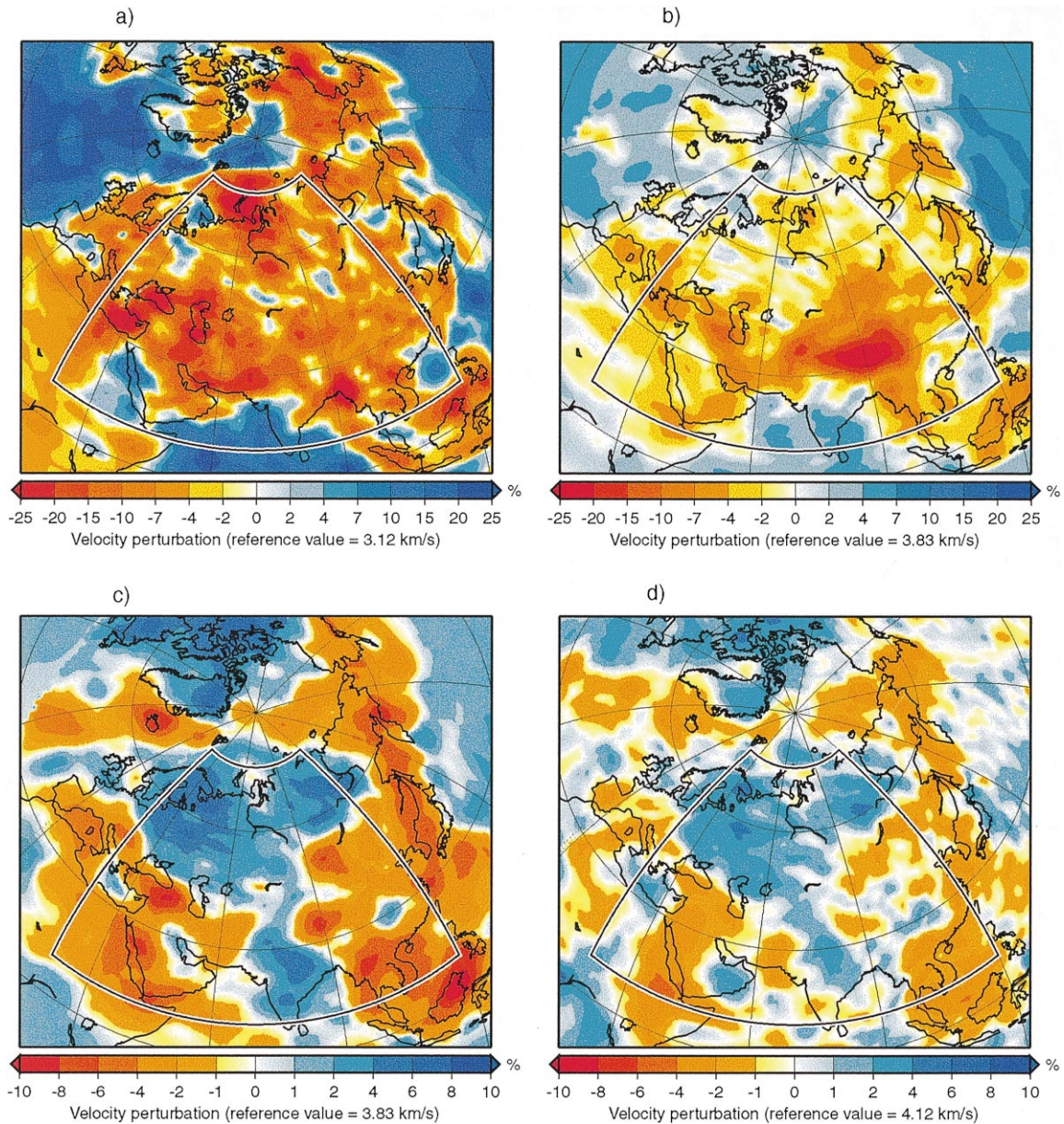
Fig. 3. Examples of group and phase velocity maps obtained by tomographic inversion of surface wave dispersion measurements: (a) 20 s Rayleigh wave group velocity; (b) 50 s Rayleigh wave group velocity; (c) 100 s Rayleigh wave group velocity and (d) 100 s Rayleigh wave phase velocity.

3. A priori information on crustal structure

In recent years new information on global crustal structure has become available. One of the most important contributions is the global crustal model CRUST5.1 of Mooney et al. (1998). This model is on a $5° \times 5°$ grid, and for each grid point the model is parameterized in terms of a depth profile or column. The

columns are divided in two layers of sediments, and a three-layer crystalline crust, in addition to ice and water layers. Thickness, seismic wave velocities (P and S) and density are provided for each layer of the model and also for the uppermost mantle. Although the availability of this model is a great improvement, its resolution (5° cells) is not optimal for regional studies, and some large features are not present in the model (e.g. the Tarim basin).

Laske and Masters (1997) have recently compiled a new global sediment model on a $1° \times 1°$ grid. Sedimentary cover in this model is parameterized by three layers. Layer thickness, wave velocities (P and S) and density are assigned for each model cell. The sources of the model in oceans are published digital high-resolution maps, averaged for each $1° \times 1°$ cell. In oceanic basins for which such digital maps are not available (e.g. the Arctic and North Atlantic), the sediment thickness was hand-digitized using atlases and maps. The sediment thickness in most of the continental areas was obtained by digitizing the tectonic map of the world (EXXON Production Research Group, 1985).

In addition to global maps, more detailed regional maps and models are available for Eurasia. The Russian Institute of Physics of the Earth (IPE) has published contour maps of sediment and crustal thickness for most of Eurasia (Kunin et al., 1987). We received these maps in digital form from the Cornell Digital Earth project (Seber et al., 1997). Recently a new model of crustal thickness over part of Eurasia has become available, as part of an effort of obtain a global model on a finer grid (G. Laske, personal communication, 1999). This $1° \times 1°$ model utilizes recent data from seismic profiles in Eurasia, but contains gaps in regions where no seismic refraction data are available (e.g. Afghanistan, Pakistan and Mongolia).

These a priori models of crustal structure are very important for obtaining our shear velocity model. Because the problem of inverting surface wave velocities for shear structure is non-linear, we linearize the problem and solve it iteratively. In this case, to guarantee the convergence of the method to the global minimum solution, it is important to have a good starting model. Some parameters of the a priori models, such as crustal and sediment thickness, are usually well constrained, especially in regions that have been the target of extensive active source seismic experiments.

Other parameters, such as sediment and crystalline crust velocities are, in general, less well know. This knowledge of the properties of the starting model can also be used in the inversion procedure. Variables that are well known a priori can be tightly constrained to remain near their starting or reference values, while constraints on other variables can be loosened.

4. Inversion method

We parameterize our three-dimensional shear velocity model in terms of one-dimensional, depth-dependent velocity profiles determined at each node of a $2° \times 2°$ grid. In this point-by-point inversion, the data are the values at each grid point of spatially smoothed group and phase velocity maps for Rayleigh and Love waves at all periods. Each depth profile is divided into four layers: sediments, crystalline crust, uppermost mantle (Moho – 220 km), and upper mantle (220–400 km), as shown in Fig. 4. Surface topography, and water and ice layers are also considered in the model, but their thickness and velocity are kept constant. For an isotropic parameterization, the model variables estimated in the inversion are: sediment velocity (constant), basement topography, crystalline crust velocity (constant and slope), Moho topography, uppermost mantle velocity (constant and slope), and velocity between 220 and 400 km. He have chosen this simple parameterization in order to enhance the resolving power of the data while maintaining a physically reasonable model. However, from long range seismic profiles there is evidence for fine-scale stratification in the uppermost mantle (Pavlenkova, 1996; Thybo and Perchuc, 1997) while our parameterization consists of a single layer between Moho and 220 km depth with a constant velocity gradient. On the other hand, surface waves have limited sensitivity to vertical velocity variations and we cannot expect to resolve fine-scale structures such as thin layers. This limitation could be reduced by introducing other types of data in the inversion (e.g. receiver functions) that have better vertical resolution. However, in this study, which uses only surface wave velocities, we favor the simpler parameterization although we must be aware of its shortcomings.

This simple isotropic parameterization is unable to fit simultaneously the long period Love and Rayleigh
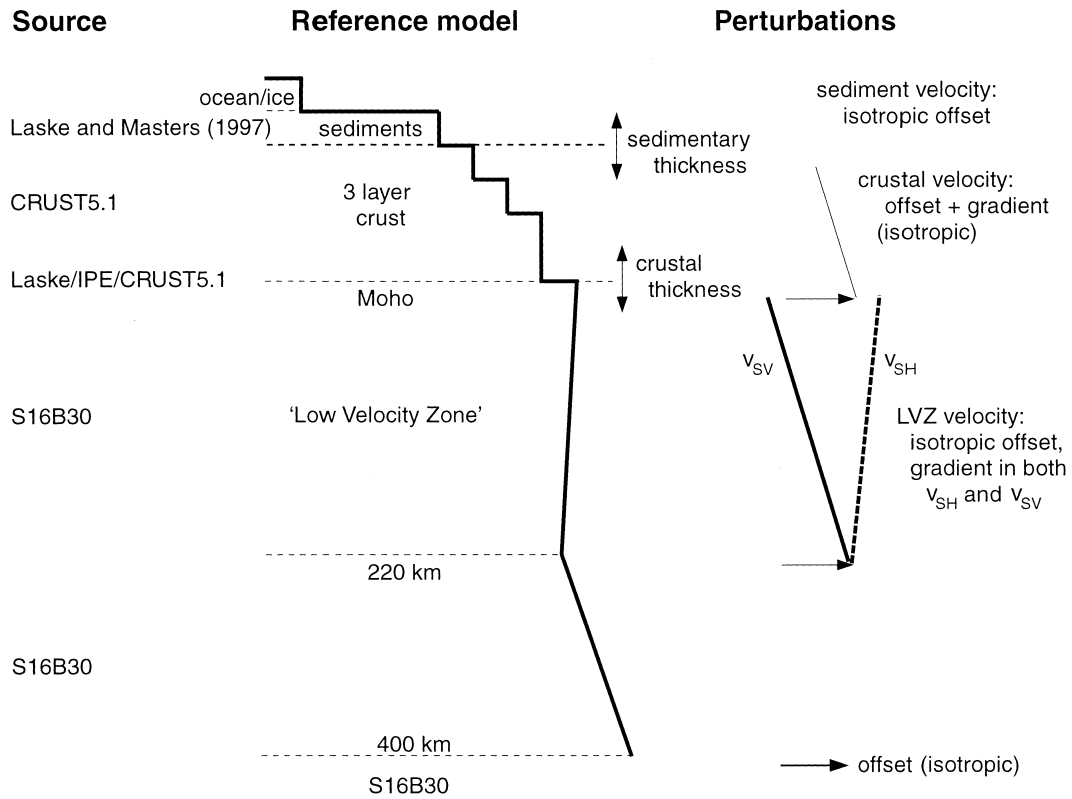
Source   **Reference model**   **Perturbations**

Fig. 4. Parameterization of the shear velocity model. A one-dimensional velocity profile is estimated for each node of the $2° \times 2°$ geographic grid.

wave data in large regions in Eurasia. The existence of this discrepancy between long period Love and Rayleigh wave data in continental regions is well known, although, its cause is still poorly understood. Many studies have addressed the discrepancy by allowing transverse isotropy in the uppermost mantle (e.g. McEvilly, 1964; Dziewonski and Anderson, 1981; Gaherty and Jordan, 1995). Other studies find that isotropic models, normally consisting of many thin layers in the uppermost mantle, are also able to fit simultaneously Love and Rayleigh wave data (Mitchell, 1984). We have chosen the transversely isotropic parameterization because it is the simplest one that fits the Rayleigh and Love data, and that can be resolved with our available dataset. We incorporate transverse isotropy in our parameterization, by introducing two shear velocities, v_{SH} and v_{SV}, between Moho and 220 km depth, with the constraint that $v_{SH} = v_{SV}$ at 220 km (Fig. 4). This parameterization

of transverse isotropy, similar to PREM for shear wave velocities, is extremely simple and does not allow for small-scale vertical variations in transverse isotropy. In spite of its limitations, this parameterization is able to provide a good fit to Rayleigh and Love surface wave data. Rayleigh waves are dominantly sensitive to variations in v_{SV}, although they are moderately affected by variations in v_{PH}, v_{PV} and η. Similarly, Love waves are dominantly sensitive to v_{SH}, but they also have non-zero sensitivity to v_{SV}. The dispersion curves are calculated including all parameters for a transversely isotropic medium (v_{SH}, v_{SV}, v_{PH}, v_{PV}, η), therefore, there are no significant approximations in the forward problem. However, in order to stabilize the inversion we only allow perturbations in v_{SH} and v_{SV}. This approximation is well justified given the small influence of perturbations in the other elastic parameters in Love and Rayleigh wave velocities. These elastic parameters (v_{PH}, v_{PV}, η) are recomputed

in each iteration using relationships between them obtained from PREM. Therefore, the introduction of transverse isotropy very approximately decouples the Love and Rayleigh wave velocities for long periods, allowing the inversion to fit them simultaneously. The inversion method uses the general linear inverse approach (e.g. Wiggins, 1972).

The starting model for the inversion is a combination of a priori crustal and mantle models. Sediment thickness and velocities are obtained from the global map of Laske and Masters (1997). Where available, we use the new Eurasia crustal thickness map (G. Laske, personal communication, 1999), and we fill the gaps with the IPE map of crustal thickness (Kunin et al., 1987; Seber et al., 1997) and CRUST5.1 (Mooney et al., 1998). The resulting reference models of sediment and crustal thickness are shown in Fig. 5. The inversion method also allows to impose limits on the maximum variation of some of the estimated parameters (e.g. thickness and velocity of crustal layers). In most of central Eurasia it is reasonable to assume that sediment and crustal thickness are known with uncertainties of less than 5 km. Therefore, during inversion we only allow changes in layer thickness smaller than 5 km. Crustal velocities are less well known, and therefore, we impose no constraints in their estimated values. The starting model for the mantle is obtained from the global 3D model S16B30 (Masters et al., 1996) by applying the S-wave velocity perturbations in S16B30 to isotropic PREM (Dziewonski and Anderson, 1981). Using this compilation of a priori information, for each point in our $2° \times 2°$ grid we construct a starting depth profile, following the parameterization shown in Fig. 4. The starting model is isotropic ($v_{SH} = v_{SV}$) but during the inversion, transverse isotropy will be introduced between the top of the mantle (below Moho) and 220 km depth.

5. Results

Fig. 6 shows a typical example of the inversion results and data fit. The estimated models shown here correspond to a grid node located in western Mongolia (48°N, 95°E), using isotropic and transversely isotropic parameterizations in the uppermost mantle. The estimated isotropic model (Fig. 6a) is unable to fit simultaneously the Love and Rayleigh
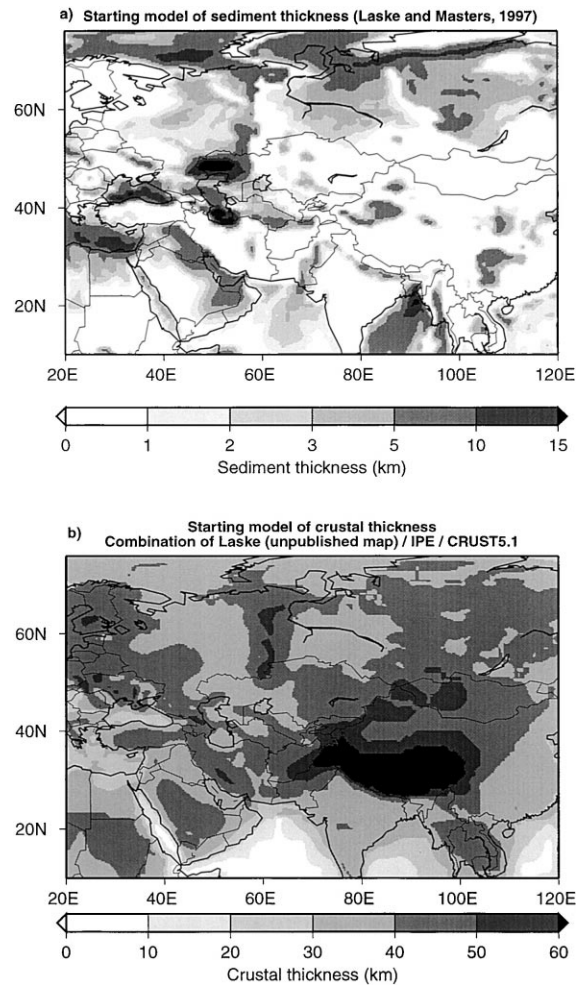

Fig. 5. A priori crustal information used as starting/reference model for the shear velocity inversion: (a) sediment thickness model of Laske and Masters (1997) and (b) crustal thickness model obtained by combining regional models for Eurasia (Kunin et al., 1987; G. Laske, personal communication) and global models (Mooney et al., 1998).

wave data, although it develops a prominent low velocity zone below the Moho in the attempt to do so. The model fits Love wave group velocities well but overestimates Rayleigh wave velocities between 40 and 100 s (Fig. 6a, top right panel). Interestingly, the situation is reversed for phase velocities: the model fits the long period Rayleigh data (80–150 s) well, but under-predicts long period Love wave velocities.

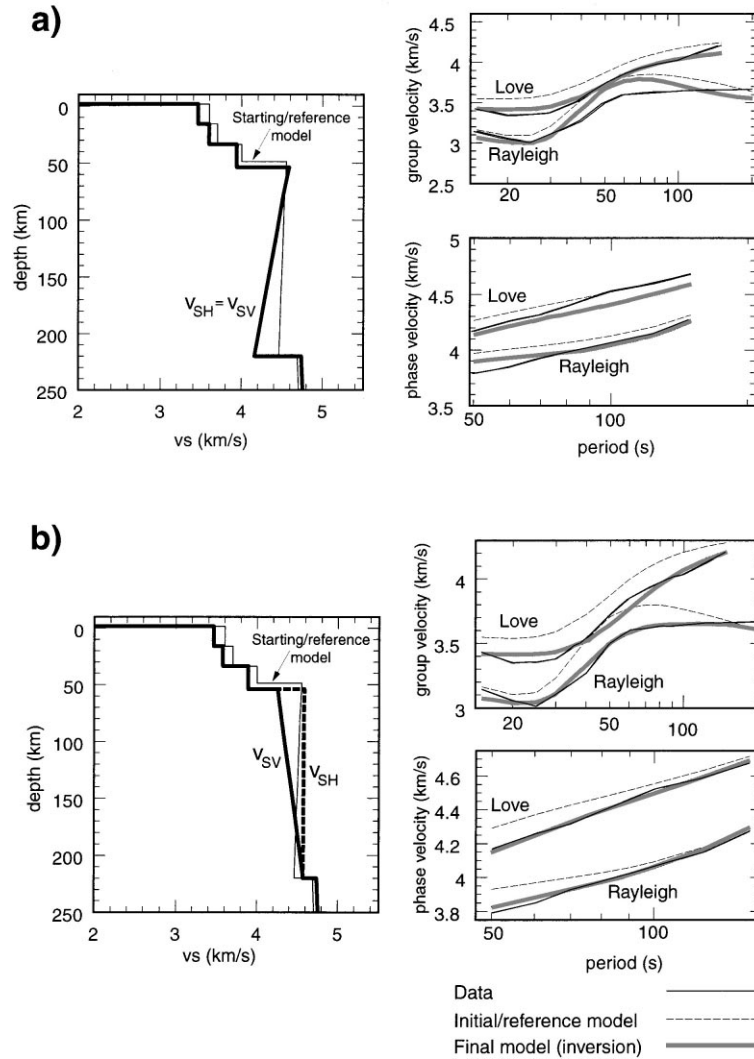Transverse isotropy has been invoked in previous studies to explain this Love–Rayleigh wave

Fig. 6. Inversion results and data fit for a point in western Mongolia with coordinates 48°N, 95°E: (a) isotropic model parameterization ($v_{SH} = v_{SV}$). The left panel shows the starting and final (after inversion) models. The top right panel shows the data fit for group velocities (period band 20–200 s), and the bottom right panel shows the data fit for phase velocities (period band 50–150 s). The thin solid lines represent the data, the thin dashed lines show the predictions from the starting model, and the thick gray lines are the result of the inversion; (b) transversely isotropic parameterization ($v_{SH} \neq v_{SV}$ between Moho and 220 km depth, and isotropic for all other depths). Symbols as in previous panels.

discrepancy for periods relevant to the upper 200 km or so of the mantle (e.g. Dziewonski and Anderson, 1981). The introduction of two velocities in this depth range, v_{SH} for horizontally polarized S waves and v_{SV} for vertically polarized S waves, effectively decouples the two data types, because Rayleigh waves are sensitive mostly to v_{SV} while Love waves are sensitive

mostly to v_{SH}. Fig. 6b shows the inversion results and data fit for a transversely isotropic parameterization. In the region between Moho and 220 km depth, $v_{SH} > v_{SV}$ and a low velocity zone is present in v_{SH} but not in v_{SV}. This parameterization substantially improves data fit, as shown in Fig. 6b. Love and Rayleigh wave velocities are now fit simultaneously, although the

model still underestimates Love wave group velocities between 50 and 60 s. We have adopted this transversely isotropic parameterization for all grid points in the model. Our goal is to define a simple model parameterization, while maintaining a physically reasonable model. For the model described in this section, eight parameters are estimated for each depth profile based on 44 data points (surface wave velocities).

Comparisons between surface wave group and phase velocity maps and predicted maps from the estimated shear velocity model provide a qualitative estimate of the data fit. Fig. 7 shows maps for 50 s Rayleigh wave group velocities and 100 s Rayleigh wave phase velocities, and theoretical maps calculated from our estimated shear velocity model. The agreement between the maps and model predictions is good in most areas, particularly for long-wavelength features.

The resolution of the shear velocity model (depth profile) at a given grid point depends on the resolution
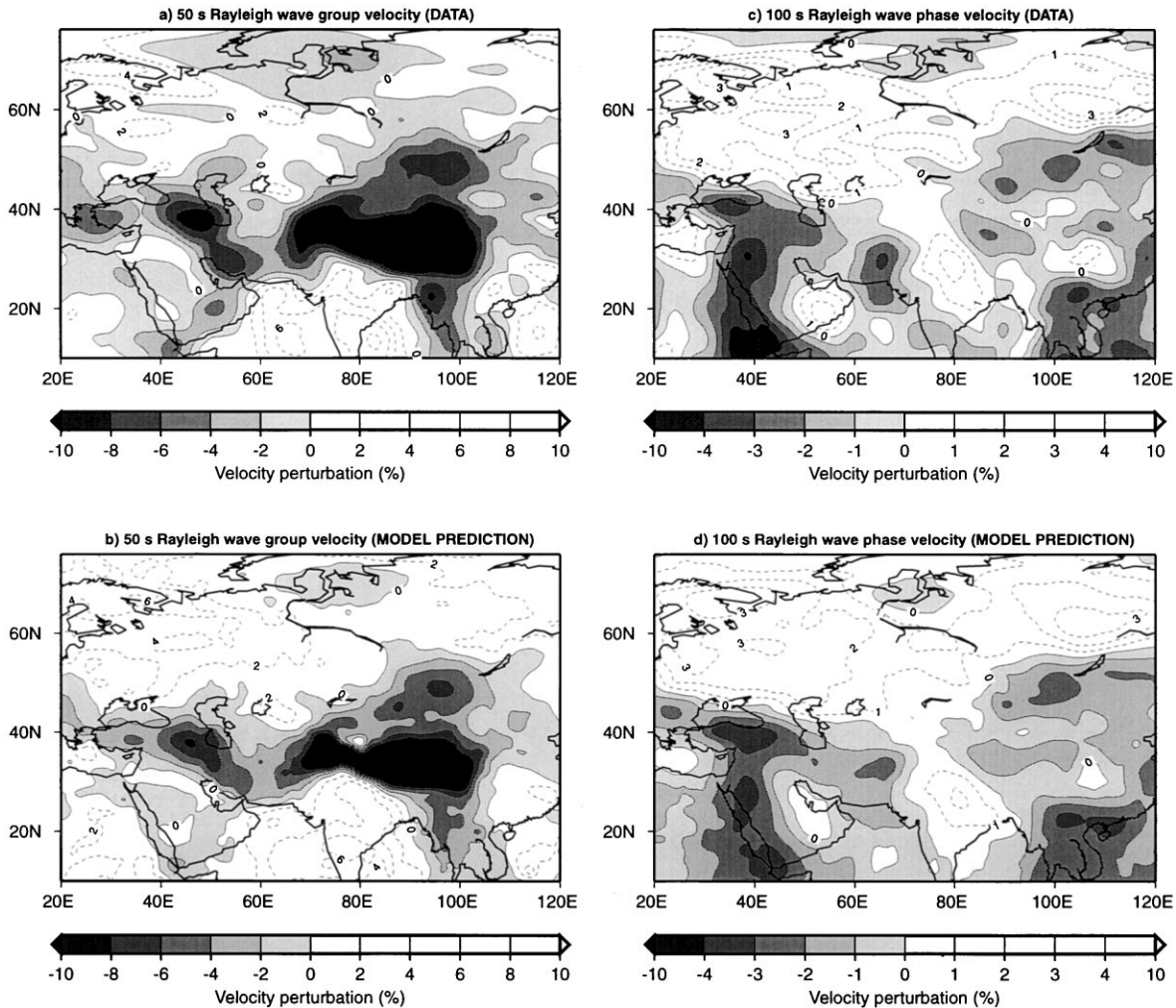

Fig. 7. Comparison between surface wave group and phase velocity maps (data) and predictions from the shear velocity model obtained in this study. Negative velocity perturbations are represented by shades of gray and positive perturbations are shown in white with dashed-line contours: (a) group velocity map for 50 s Rayleigh waves (data); (b) model predictions; (c) phase velocity map for 100 s Rayleigh waves (data) and (d) model predictions.

and quality of the surface wave velocity maps for that point. Maps for each period and wave type have different spatial resolutions depending on the path density, azimuthal coverage and quality of the measurements used (see Fig. 2). For group velocities, coverage is very high inside the model region (box in Fig. 2), but decreases across the Arabian peninsula and southern India. Path density for phase velocities is in general lower than for group velocities (50 ray paths for each $2° \times 2°$ node on average; Fig. 2). The Arabian peninsula and southern India are also regions of lower phase velocity path coverage, so we expect lower quality of the shear velocity model in these areas. Path density and azimuthal coverage are fairly good for the rest of the model. Because the inversion procedure is on a point-by-point basis and the surface wave velocity maps extend well beyond the model boundaries, edge effects do not occur. In terms of depth resolution, a degradation is expected below 220 km because of the number and quality of measurements decrease toward longer periods, especially for Love waves.

The crustal part of the shear velocity model is presented here as maps of sediment and crustal thickness (Fig. 8). Estimates of sediment and crustal thickness after inversion are similar to the starting values, and all major sedimentary basins are present in the final model. This is a predictable result because low velocity features associated with major basins are clearly present in the short period surface wave velocity maps (e.g. Ritzwoller and Levshin, 1998). Crustal thicknesses beneath the Himalayas, Hindu–Kush, Tibetan Plateau and Tien Shan are not significantly changed relative to the starting model. However, in the Caucasus, Urals and Zagros the estimated crustal thickness is smaller than the starting model, resulting in less prominent crustal roots for these regions (Fig. 8b). This result only indicates that crustal roots beneath these regions are not required to fit the surface wave data, but the existence of these roots is well documented, particularly in the Urals, from a large number of active-source seismic profiles.

The upper mantle velocity structure (v_{SV}) at a depth of 100 km is shown in Fig. 9a. Perhaps the most prominent features of the model are the high velocity anomalies associated with the east European platform, Siberian platform, and northern Indian shield. Some other positive anomalies smaller in extent are found beneath large sedimentary basins: eastern Mediter-
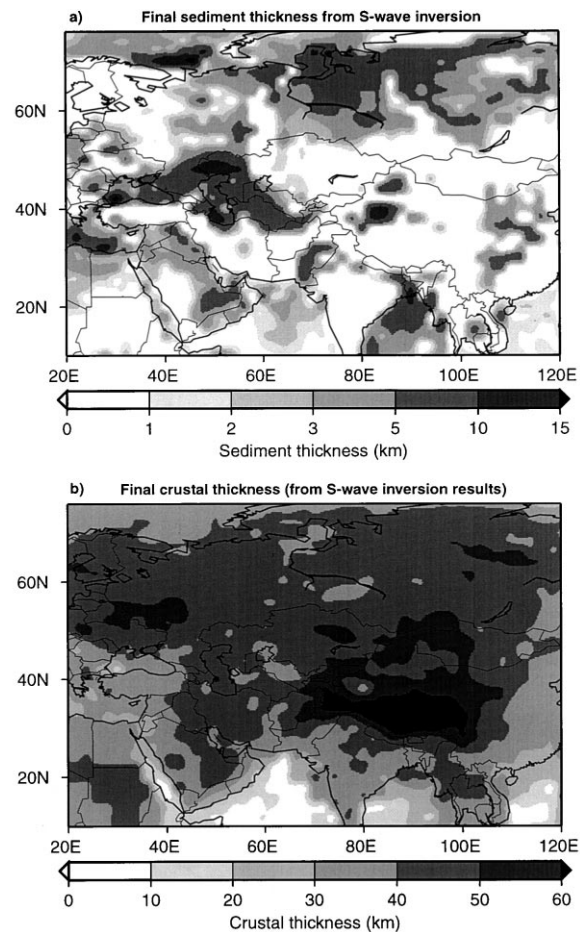

Fig. 8. Inversion results for (a) sediment and (b) crustal thicknesses. Compare results with starting/reference model (Fig. 5).

ranean, Caspian Depression, Persian Gulf, and Tarim basin. Low velocities are associated with a segment of the Alpine–Himalaya collision zone extending from Turkey to Iran and Afghanistan. The western Arabian peninsula, Red Sea, and the Afar triangle region in northeast Africa are also underlain by large low velocity anomalies. Large low velocity regions also extend beneath Indo-China and the south China Sea, and beneath Mongolia, with its largest anomalies occurring southwest of lake Baikal. Smaller low velocity anomalies can also be found in northern Tibet, and south of lake Balkhash in Kazakhstan.

For comparison, Fig. 9b shows the *S* velocity model of Bijwaard et al. (1998), obtained by inversion of

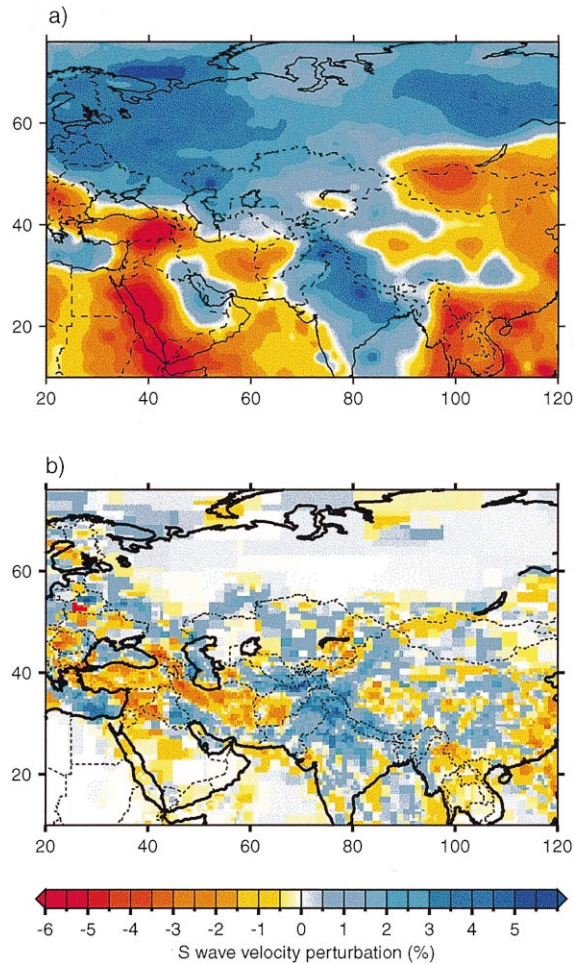a)

b)

S wave velocity perturbation (%)

Fig. 9. Shear velocity structure in the uppermost mantle (horizontal slice at 100 km depth): (a) v_{SV} velocity obtained in this study by inversion of surface wave velocities; (b) v_s model of Bijwaard et al. (1998) obtained by inversion of S-wave arrival times.

The strength and distribution of transverse isotropy is shown in Fig. 10 as the difference between v_{SH} and v_{SV} at 80 km depth. Values greater than zero indicate transverse isotropy with $v_{SH} > v_{SV}$ and negative values indicate reverse anisotropy in which $v_{SV} > v_{SH}$. Because of our parameterization, the difference between v_{SV} and v_{SH} is largest just beneath Moho and decreases to zero at 220 km depth. This situation is analogous to PREM for which the difference $v_{SH} - v_{SV}$ just beneath Moho is 0.22 km/s, equivalent to an intrinsic anisotropy of ∼4.8%. At 80 km depth, the difference $v_{SH} - v_{SV}$ for PREM is 0.15 km/s or ∼3.4%. As can be seen in Fig. 10, the mantle beneath Eurasia is transversely isotropic with average values similar to PREM. Regions of larger than average anisotropy are also found beneath north and central Tibet, Afghanistan and Burma. Anisotropy is large in the western Arabian peninsula but, because of the decrease in path density and azimuthal coverage of the surface wave velocity maps in this area, these values are poorly constrained and could also be affected by bias due to azimuthal anisotropy. Bias due to azimuthal anisotropy is generally small, but increases in regions in the periphery of the group and phase velocity maps (Ritzwoller and Levshin, 1998). The reliability of the v_{SH} model is in general lower than the v_{SV} model due to the smaller number and quality of the Love wave data at long periods. In addition, the existence of reverse anisotropy ($v_{SV} > v_{SH}$) is questionable, occurring predominantly in regions where the long period group and phase velocity maps are inconsistent (e.g. in the East European platform). We expect that the incorporation of additional phase and group velocity data will improve the agreement between the maps and eliminate these anomalous regions.

The existence of a low velocity zone (LVZ) is determined by the sign of the vertical gradient of v_{SH} and v_{SV} between Moho and 220 km depth. A negative velocity gradient indicates a LVZ and a positive gradient indicates the absence of a LVZ. Fig. 11 shows that a LVZ in v_{SH} is pervasive across Eurasia, but is very small or absent in v_{SV}. This behavior in the uppermost mantle is consistent with PREM. Regions with a pronounced low velocity zone (greater than PREM) in v_{SH} include both mountain ranges and stable continental blocks. Tectonically active regions, including the Tibetan Plateau, Hindu–Kush and Zagros, exhibit

body wave arrival times from the dataset of Engdahl et al. (1998). The agreement is very good in regions where both models are well constrained, with most of all long-wavelength features present in both models, although, the magnitude of the velocity anomalies is generally smaller in the model of Bijwaard et al. (1998). When comparing both models we must take into account that the model of Bijwaard et al. (1998) is an isotropic model of S-wave velocity, v_s, which is unconstrained for shallow layers without seismic sources and/or receivers (e.g. the East European and Siberian cratons).

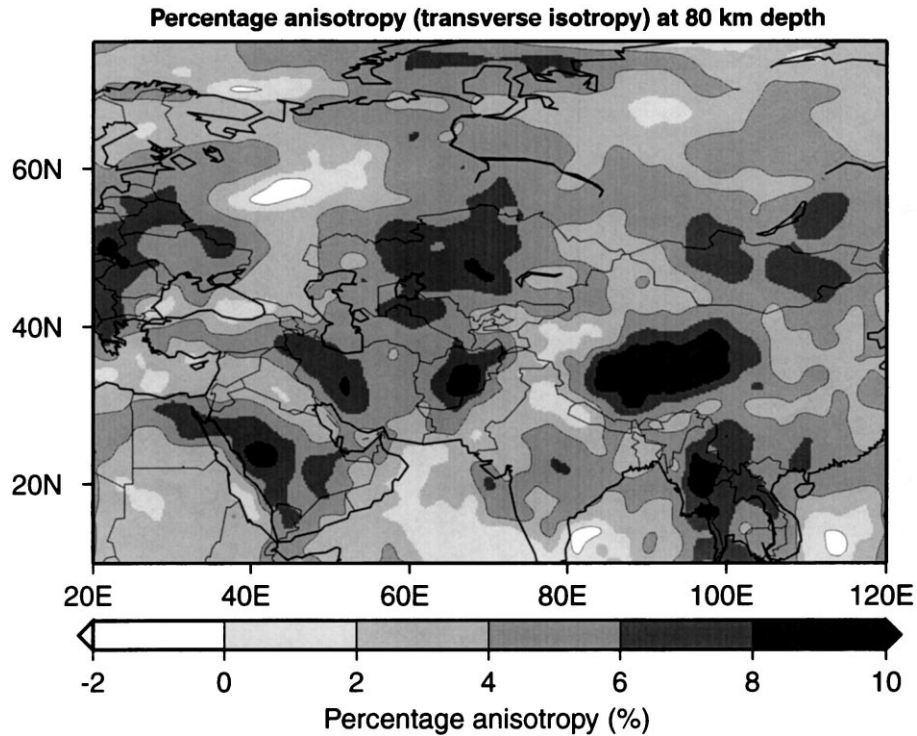**Percentage anisotropy (transverse isotropy) at 80 km depth**

Fig. 10. Strength of anisotropy (transverse isotropy) at 80 km depth. The values displayed are percentage anisotropy, defined as $200(v_{SH} - v_{SV})/(v_{SH} + v_{SV})$. Positive values indicate $v_{SH} > v_{SV}$. The percentage anisotropy value for PREM at 80 km depth is ~3.4%.

the most well developed low velocity zones. Some stable regions such as the western part of the East European platform, Kazakh platform, Arabian peninsula and Indian subcontinent also display prominent low velocity zones in v_{SH}.

6. Discussion

As shown in Fig. 9, the old, stable cratons located north of the Alpine–Himalayan orogenic belt are characterized by high upper-mantle shear velocities. High shear velocities are also found beneath the Indian shield, the southern Tibetan Plateau, and the Tarim basin (Fig. 9). While, high shear velocities in the upper mantle are usually interpreted as an indication of old, cold, thick lithospheric blocks, the structures associated with low velocity anomalies are more difficult to interpret. Large low velocity anomalies are associated with young, extensional plate boundaries,

such as the Red Sea and Andaman ridges. The low velocity anomaly beneath central and northern Tibet has received a great deal of attention (see Molnar, 1988) because of its implications for the origin and mechanism for the formation of the Tibetan Plateau. However, although clearly present in our model and in the model of Bijwaard et al. (1998), it is not one of the most prominent anomalies in magnitude or in extent. Based upon the presence of this low velocity region and other evidence (e.g. widespread Quaternary volcanism and inefficient S_n propagation) Molnar et al. (1993) proposed that the high-velocity Indian lithosphere has not been underthrusted beneath the Tibetan Plateau, and that crustal thickening has occurred by north–south shortening of southern Eurasia's crust. As a result, flow in the mantle under Tibet is probably from west to east, because it would be blocked in the west by the keel of the Tarim block. This is supported by the orientation of SKS fast polarization directions (McNamara et al., 1994) and by
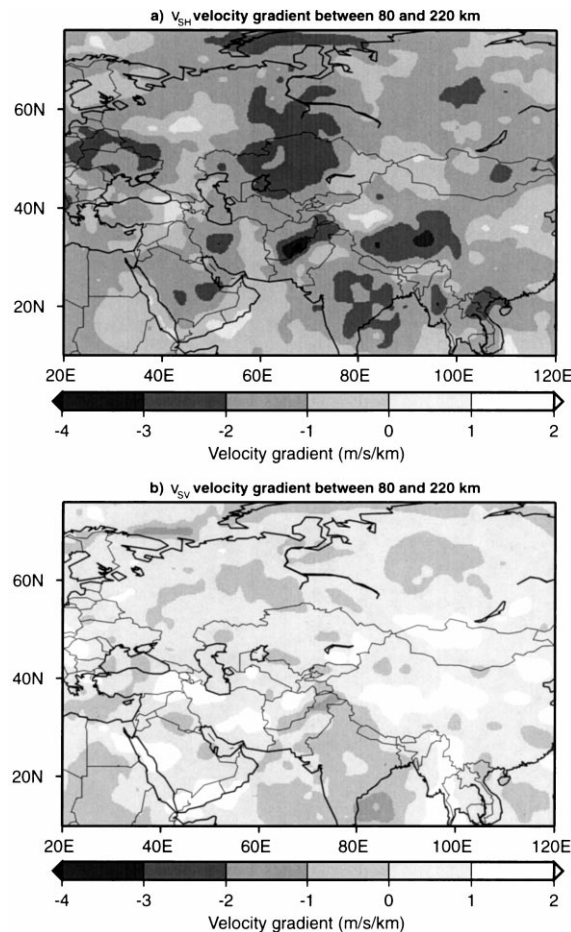
Fig. 11. Velocity gradient of the shear velocity model between Moho and 220 km depth. A positive value indicates that velocity increases with depth. A negative value indicates the existence of a low velocity zone in this depth range. Units are m/s/km: (a) velocity gradient for v_{SH} and (b) velocity gradient for v_{SV}. A low velocity zone is pervasive for v_{SH} and mostly absent for v_{SV}.

evidence of correlated crust and mantle strain fields in Tibet (Holt, 2000). Anisotropy (transverse isotropy) in our model is largest beneath Tibet (Fig. 10) although the relationship between mantle flow and the strength of transverse isotropy is poorly understood. In continents, upper-mantle anisotropy appears to be inherited from major episodes of orogenic deformation. The superposition of many such episodes results in a fabric of anisotropy that varies on a much smaller geographical scale than, for instance, in oceanic regions, where the fast-axis dominant direction is

azimuthally coherent and aligned with the direction of plate-scale flow. Long period surface waves sampling the continental uppermost mantle of Eurasia are normally measured only for long paths (over 30 or 40°), averaging out small-scale azimuthal variations in anisotropy. Therefore, the path-averaged structure can be approximated by a transversely isotropic effective medium (Gaherty and Jordan, 1995). Assuming that anisotropy in the uppermost mantle is mostly related to the orientation of olivine crystals, the predominance of $v_{SH} > v_{SV}$ throughout most of central Eurasia, suggests that the alignment of olivine crystals is mainly horizontal. The largest values of anisotropy (transverse isotropy) in our model are associated with areas of active orogenic deformation (Tibet, Hindu–Kush, Zagros) but it is also present in currently inactive areas of stable Asia, such as the Urals or the Kazakh platform (Fig. 10). Gaherty and Jordan (1995) also found significant transverse isotropy beneath the Australia craton, and proposed that this anisotropy is frozen in the uppermost lithospheric mantle.

One of the most prominent upper mantle low velocity regions is located in the middle east, extending from Turkey to Iran and western Afghanistan (Fig. 9). This low velocity anomaly coincides with the Turkish–Iranian continental plateau, formed by the collision between the Arabian and Eurasian plates. This collision is the result of the closing of the neo-Tethys ocean by northward subduction of oceanic lithosphere beneath Eurasia. In Iran and western Afghanistan, the low velocity anomaly is bounded to the south by high velocities, part of the Arabian plate. The low velocity anomaly is also a prominent feature in the global model of Bijwaard et al. (1998; Fig. 9b) and in P_n tomography studies (e.g. Hearn and Ni, 1994), and is also coincident with a region of high S-wave attenuation (Kadinsky-Cade et al., 1981) and Neogene volcanism (Kazmin et al., 1986). The combination of these observations suggests a hot or perhaps partially molten uppermost mantle beneath the Turkish–Iranian Plateau. This anomalously hot upper mantle could be a remnant of the backarc extensional regime that dominated this region from the Jurassic to the Neogene (Dercourt et al., 1986). The presence of hot, molten upper mantle weakens the lithosphere, allowing larger deformation associated with the Arabian plate-Eurasia collision. This results in the observed

diffuse intraplate seismicity that extends well to the north of the plate boundary delineated by the Zagros Main Thrust. Furthermore, the buoyancy associated with hot upper mantle, combined with the buoyancy due to the deep continental roots in the region, can contribute to maintain the high topography of the plateau.

Another significant upper-mantle low velocity anomaly is centered in western Mongolia, WSW of lake Baikal (Fig. 9). The central part of this anomaly coincides with the Hangay Dome area of central Mongolia. The Hangay Dome is characterized by recent uplift, diffuse extension and regionally up-warped topography (Cunningham, 1998). This is also a region of recent Cenozoic volcanism and high heat flow (with a maximum of approximately 80 mW/m^2). There is a remarkable agreement between the shape of the velocity anomaly (Fig. 9a) and the heat flow anomaly (Fig. 5a of Cunningham, 1998). This region in Mongolia has been interpreted to overlie a mantle plume or asthenospheric diapir, which is associated with rifting in lake Baikal (Windley and Allen, 1993). Lake Baikal is located at the boundary between the Mongolian Plateau and the Siberian Craton, which is consistent with the marked contrast between low and high velocities observed in our shear velocity model (Fig. 9). Deformation due to the presence of the mantle plume or asthenospheric diapir manifests in high seismic activity in western Mongolia, which has been the site of some of the largest ($M \geq 8$) intraplate earthquakes recorded during this century (i.e. 1905 and 1957).

Acknowledgements

References

Barmin, M.P., Levshin, A.L., Ritzwoller, M.H., 2000. Regional surface wave tomography. Pure Appl. Geophys., in press.

Bijwaard, H., Spakman, W., Engdahl, E.R., 1998. Closing the gap between regional and global travel time tomography. J. Geophys. Res. 103, 30055–30078.

Cunningham, W.D., 1998. Lithospheric controls on late Cenozoic construction of the Mongolian Altai. Tectonics 17, 891–902.

Dercourt, J., et al., 1986. Geological evolution of the Tethys belt from the Atlantic to the Pamirs since the Lias. Tectonophysics 123, 241–315.

Dziewonski, A.M., Anderson, D.L., 1981. Preliminary reference Earth model. Phys. Earth Planet. Int. 25, 297–356.

Engdahl, E.R., van der Hilst, R., Buland, R., 1998. Global teleseismic earthquake relocation with improved travel times and procedures for depth determination. Bull. Seism. Soc. Am. 88, 722–743.

EXXON Production Research Group, 1985. Tectonic map of the world.

Gaherty, J.B., Jordan, T.H., 1995. Lehmann discontinuity as the base of an anisotropic layer beneath continents. Science 268, 1468–1471.

Hearn, T.M., Ni, J.F., 1994. P_n velocities beneath continental collision zones: the Turkish–Iranian plateau. Geophys. J. Int. 117, 273–283.

Holt, W.E., 2000. Correlated crust and mantle strain fields in Tibet. Geology 28, 67–70.

Kadinsky-Cade, K., Barazangi, M., Oliver, J., Isacks, B., 1981. Lateral variations of high-frequency seismic wave propagation at regional distances across the Turkish and Iranian Plateaus. J. Geophys. Res. 86, 9377–9396.

Kazmin, V.G., Sbortshikov, I.M., Ricou, L.E., Zonenshain, L.P., Boulin, J., Knipper, A.L., 1986. Volcanic belts as markers of the Mesozoic–Cenozoic active margin of Eurasia. Tectonophysics 123, 123–152.

Kunin, N.Y., et al., 1987. Basement surface relief map. Institute of Physics of the Earth. Academy of Sciences, Ministry of Geology of the Russian Federation, Moscow.

Laske, G., Masters, G., 1997. A global digital map of sediment thickness. Eos Trans. AGU 78 F483 (Abstract).

Levshin, A.L., Ratnikova, L., Berger, J., 1992. Peculiarities of surface wave propagation across central Eurasia. Bull. Seism. Soc. Am. 82, 2464–2493.

Masters, G., Johnson, S., Laske, G., Bolton, H., 1996. A shear-velocity model of the mantle. Phil. Trans. R. Soc. London A 354, 1385–1411.

McEvilly, T.V., 1964. Central US crust — upper mantle structure from Love and Rayleigh wave phase velocity inversion. Bull. Seism. Soc. Am. 54, 1997–2015.

McNamara, D.E., Owens, T.J., Silver, P.G., Wu, F., 1994. Shear wave anisotropy beneath the Tibetan Plateau. J. Geophys. Res. 98, 12003–12017.

Mitchell, B.J., 1984. On the inversion of Love- and Rayleigh-wave dispersion and implications for Earth structure and anisotropy. Geophys. J. R. Astr. Soc. 76, 233–241.

Molnar, P., 1988. A review of geophysical constraints on the deep structure of the Tibetan plateau, the Himalaya and the Karakoram, and their tectonic implications. Phil. Trans. R. Soc. London A326, 33–88.

Molnar, P., England, P., Martinod, J., 1993. Mantle dynamics, uplift of the Tibetan Plateau, and the Indian monsoon. Rev. Geophys. 31, 357–396.

Mooney, W.D., Laske, G., Masters, T.G., 1998. CRUST5.1: a global crustal model at $5° \times 5°$. J. Geophys. Res. 103, 727–747.

Pavlenkova, N.I., 1996. General features of the uppermost mantle stratification from long-range seismic profiles. Tectonophysics 264, 261–278.

Ritzwoller, M.H., Levshin, A.L., 1998. Eurasian surface wave tomography: group velocities. J. Geophys. Res. 103, 4839–4878.

Searle, M.P., Windley, B.F., Coward, M.P., Cooper, D.J.W., Rex, A.J., Rex, D., Tingdong, L., Xuchang, X., Jan, M.Q., Thakur, V.C., Kumar, S., 1987. The closing of Tethys and the tectonics of the Himalaya. Geol. Soc. Am. Bull. 98, 678–701.

Seber, D., Vallve, M., Sandvol, E.A., Steer, D.N., Barazangi, M., 1997. Middle east tectonics applications of geographic information systems (GIS). GSA Today 7, 1–6.

Thybo, H., Perchuc, E., 1997. The seismic 8° discontinuity and partial melting in continental mantle. Science 275, 1626–1629.

Trampert, J., Woodhouse, J.H., 1995. Global phase velocity maps of Love and Rayleigh waves between 40 and 150 s period. Geophys. J. Int. 122, 675–690.

Wessel, P., Smith, W.H.F., 1998. New, improved version of the generic mapping tools released. Eos Trans. AGU 79, 579.

Wiggins, R.A., 1972. The general linear inverse problem: implication of surface waves and free oscillations for Earth structure. Rev. Geophys. Space Phys. 10, 251–285.

Windley, B.F., Allen, M.B., 1993. Mongolian plateau: evidence for a late Cenozoic mantle plume under central Asia. Geology 21, 295–298.

Yanovskaya, T.B., Ditmar, P.G., 1990. Smoothness criteria in surface wave tomography. Geophys. J. Int. 102, 63–72.